Near-surface microstructure of Ni-23 at. % Pt: Grazing incidence diffraction and first-principles calculations

M. Engelke,[1] B. Schönfeld,[1] and A. V. Ruban[2]
[1]*Laboratory of Metal Physics and Technology, Department of Materials, ETH Zurich, 8093 Zurich, Switzerland*
[2]*Department of Materials Science and Engineering, KTH, Stockholm, Sweden*
(Received 7 September 2009; revised manuscript received 27 November 2009; published 4 February 2010)

Diffuse x-ray scattering under grazing incidence was measured of a Ni-23.2 at. % Pt(110) surface at 923 K. The modulation of in-plane and out-of-plane scattering is characterized by the maxima in short-range order scattering located at positions of the X type (as for the bulk microstructure). The Warren-Cowley short-range order parameters from diffuse scattering are in good agreement with theoretical simulations based on bulk effective pair interaction parameters from first-principles theory. The nearest-neighbor interaction parameter is dominant also when determined from short-range order scattering. Its value is larger than for the bulk microstructure of Pt-rich alloys, what might reflect the difference in composition and is not compellingly due to the near-surface microstructure. Allowing for the presence of a tetragonal site occupation, indications for a segregation profile are weak in diffuse scattering and hardly resolvable for the Warren-Cowley short-range order parameters. This is consistent with the findings for layer-resolved short-range order parameters from theory. Theoretical simulations also demonstrated that the strong Ni enrichment of the surface layer has the same origin as the segregation reversal for the (110) surface in the case of Ni-50 at. % Pt.

DOI: 10.1103/PhysRevB.81.054205 PACS number(s): 61.66.Dk, 68.47.De, 64.60.Cn

I. INTRODUCTION

Surfaces of Ni-Pt alloys have attracted much interest because of their catalytic potential. Both, Ni and Pt, exhibit specific catalysis properties and the idea of modifying these properties by alloying appears attractive (see Ref. 1 for a review on Pt-alloy surfaces). The most striking feature of Ni-Pt surfaces is the segregation reversal among low-index planes with Ni enrichment in the top layer of the (110) surface but Pt enrichment for (100) and (111) surfaces. The subsequent layers show an oscillatory segregation profile as found typically with locally ordered alloys.[2,3]

Because of the large size difference between the Ni and Pt atoms amounting to about 11%, interplanar relaxation is connected with the segregation profile. For Ni-50 at. % Pt, e.g., the two top interplanar spacings of the open (110) surface deviate by −19% and 11% from those in the bulk while there is a contraction of just 2% for both top interplanar spacings with the close-packed (111) surface.[2,3] With increasing Ni fraction the interplanar relaxation of (110) and (111) surfaces decreases as seen for Ni-10 at. % Pt.[4,5]

Reconstruction is known to appear for pure Pt, not for pure Ni. In the case of Ni-Pt alloys, superstructures corresponding to (12×1) and (19×1) reconstructions were observed for the Ni-50 at. % Pt(100) surface with a quasihexagonal atomic mesh.[1] (see also Ref. 6 for Ni-40 at. % Pt) For Ni-25 at. % Pt(100), a local reconstruction with shifted rows was found.[7] No investigations were performed for the (110) and (111) surfaces.

The experimental methods for surface analysis mainly comprised low-energy electron diffraction (LEED), low- and medium-energy ion scattering (LEIS, MEIS), also in combination with shadowing and blocking, incidence-dependent excitation for Auger spectroscopy (IDEAS), and scanning tunneling microscopy (STM).[1–8] Information from any such analysis is restricted to the first few top layers. The atomic arrangement from a deeper region, that still might differ from the bulk microstructure, is accessible if diffuse scattering under grazing incidence is employed. Elastic diffuse scattering with x rays and neutrons may be used that has proven to be a fruitful tool in characterizing the bulk microstructure (for reviews, see Refs. 9–13). Then the near-surface microstructure comprising a few ten layers may be analyzed.

Diffuse x-ray scattering experiments under grazing incidence with a quantitative evaluation of the near-surface microstructure were until now only reported for Cu-25 at. % Au (Ref. 14) and Pt-48 at. % Rh (Ref. 15). These investigations under grazing incidence were restricted to in-plane diffuse scattering. Thus, only two-dimensional (2D) Fourier coefficients or a restricted number of three-dimensional (3D) Fourier coefficients of local order could be determined. More detailed information also requires out-of-plane diffuse scattering to be measured. Furthermore, if a strong segregation profile and thus a distinct direction is present, an orthorhombic anisotropic site occupation (instead of a cubic isotropic one as used for a cubic bulk microstructure) might be better suited.

In the present investigation a Ni-23.2 at. % Pt(110) surface in a state of thermal equilibrium above the order-disorder transition temperature (i.e., a solid solution is present) was selected. This composition was preferred over Ni-50 at. % Pt, as the transition temperature is lower and there is a cubic to cubic order-disorder transition, no reconstruction is known that will render data evaluation more complex, and a distinct direction is still expected because of the lattice plane relaxation for the open (110) surface.

In this investigation a technique that has been successful in determining the (homogeneous) bulk microstructure, will be applied to characterize a region where heterogeneities in displacements and atomic arrangements are present. The microstructural heterogeneity will be reflected in diffuse scattering in an indirect way, as averaged pair correlations are

extracted. No direct comparison with the bulk microstructure is available for the given composition, only for states close to the Ni-Pt 1:1 and 1:7 stoichiometries.[16–18]

Much information is available for Ni-50 at. % Pt. Here, theory was successful to describe the (111) and (110) segregation profiles known experimentally (see Gauthier[1] and references therein), the Warren-Cowley short-range order parameters of Saha and Ohshima[16] and the order-disorder transition temperature in the bulk. It was also shown that interaction parameters do not differ much between the bulk and near the surface.

The experimentally well-established segregation reversal among the three low-index surfaces of Ni-Pt has attracted the interest of theoreticians.[19–22] The origin of this phenomenon had been identified in *ab initio* calculations first by Abrikosov *et al.*,[20] and later confirmed by Pourovskii *et al.*[22] In particular, it was found that Pt segregation was actually preferable on all three low-index surfaces, including the (110) surface, if only the segregation energy was taken into consideration. The segregation reversal on the (110) surface was attributed to the fact that the segregation energy of Pt into the second layer of this surface was much lower than to the first. Thus, Pt segregated actually to the subsurface layer and then the strong ordering effective interactions at the first coordination shell led to the Pt depletion in the first and third surface layer.

The work by Abrikosov *et al.*[20] was based on the Connolly-Williams-type cluster expansion of the surface energy of a random Ni-50 at. % Pt alloy. The effective interactions obtained in this way were coefficients of expansion of the surface energy of an alloy in terms of the layer concentrations rather than the 'real effective interactions' which can be associated with atomic ordering on the lattice. Nevertheless, the use of such interactions in the consequent single-site mean-field simulations of the concentration profile was justified since the atomic short-range order was neglected in such a consideration.

The later work of Pourovskii *et al.*[22] has improved on several issues relative to the work by Abrikosov *et al.*[20] First of all, the pair and higher-order effective cluster interactions in this work were obtained by the screened generalized perturbation method (SGPM) (Refs. 23 and 24) and therefore it was possible to perform more accurate thermodynamic simulations. Second, the attempt was made to take into consideration local relaxation effects in random alloys, whose energetics had been ignored by Abrikosov *et al.*,[20] and which should have a strong effect on the alloy energetics and configuration. Finally, the grand-canonical Monte Carlo method was used to calculate the surface concentration profile of the (111) and (110) surfaces using interactions from *ab initio* calculations. The conclusions of the work by Abrikosov *et al.*[20] about the origin of the segregation reversal still remained unaltered.

In this work, a theoretical framework similar to that used by Pourovskii *et al.*[22] is employed, with some additional features concerning the treatment of the high-temperature state of Ni-Pt and a different ansatz for the relaxation effects that are taken into consideration using the formalism of the strain-induced interactions.

II. METHODOLOGY OF THE FIRST-PRINCIPLES-BASED SIMULATIONS

A. Statistical thermodynamics method

The configurational energy of Ni-Pt alloys has been mapped onto an Ising-type Hamiltonian with concentration-independent effective cluster interactions, which, when generalized for surfaces, can be written in the following way:

$$H = \sum_{i\lambda} \tilde{V}^{(1)}_{\lambda} \sigma_{i\lambda} + \frac{1}{2} \sum_{i\lambda;j\lambda'} \tilde{V}^{(2)}_{\lambda\lambda';p(ij)} \sigma_{i\lambda}\sigma_{j\lambda'} + \frac{1}{3} \sum_{i\lambda;j\lambda';k\lambda''} \tilde{V}^{(3)}_{\lambda\lambda'\lambda'';t(ijk)} \sigma_{i\lambda}\sigma_{j\lambda'}\sigma_{k\lambda''} + \cdots, \quad (1)$$

where spin variables $\sigma_{i\lambda}$ are used that take on values 1 if site i in the λ layer is occupied by Pt and -1 if it is occupied by Ni. Here $\tilde{V}^{(1)}_{\lambda}$ is the on-site interaction in the λth layer, $\tilde{V}^{(2)}_{\lambda\lambda';p(ij)}$ the effective pair interaction (EPI) of type p between λ and λ' layers, and $\tilde{V}^{(3)}_{\lambda\lambda'\lambda'';t(ijk)}$ the three-site interaction of type t. The tilde is used to distinguish spin-variable interactions from the GPM interactions, $V^{(n)}$, defined in the concentration-variable basis, $c_i = 1/2(\sigma_i + 1)$; they are connected by $\tilde{V}^{(n)} = 2^{-n} V^{(n)}$.

The use of the concentration-independent form is very convenient for the kind of problems where the alloy composition may change. As has been pointed out in Ref. 25, such an approach is unjustified in systems where the interactions depend strongly and nonlinearly on concentration. The latter is usually the case if alloys are composed of atoms with different valence states. However, this is not the case of isoelectronic Ni-Pt alloys and this will be demonstrated below, and therefore this particular form of Eq. (1) will be used in the present theoretical simulations.

The on-site interactions can be determined for each layer from the surface energy of the equiatomic homogeneous random alloy as

$$\tilde{V}^{(1)}_{\lambda} = \frac{\partial E_{\mathrm{surf}}}{\partial \sigma_{\lambda}} \quad (2)$$

or equivalently as half the difference in the surface energies of two surface alloy systems being equiatomic and random in every layer but the λ layer: that layer should consist of pure Pt or pure Ni. On-site interactions are then normalized to have $V^{(1)}_{\lambda} = 0$ for the deep bulklike layers.

B. Electronic structure and total-energy calculations

A number of different first-principles techniques were employed in this work. In particular, bulk and surface Green's function techniques in the framework of the Korringa-Kohn-Rostoker (KKR) method in the atomic sphere approximation (ASA) combined with the coherent-potential approximation (CPA) for treating random alloys as described in Refs. 26 and 27 were used to calculate the effective cluster interactions. The locally self-consistent Green's function (LSGF) method[28,29] was used to determine on-site and intersite screening constants in random bulk and surface Ni-Pt

alloys.[30] The Green's function exact muffin-tin orbital (EMTO) method[31,32] was used in the calculations of the ground-state properties and effective interactions in Ni-Pt alloys. Finally, the full potential projector augmented wave (FP-PAW) method[33,34] as implemented in the Vienna *ab initio* simulation package (VASP) (Refs. 35 and 36) was used to determine the strain-induced interactions in Ni-Pt alloys.

All the first-principles calculations related to the effective cluster interactions were done for a lattice spacing of 3.68 Å, which is an experimental estimate at about 900 K. Note that this value is in reasonable agreement with the theoretical estimate of 3.70 Å, obtained in the Debye-Grüneisen model[37] from the generalized gradient approximation (GGA) (Ref. 38) total energies of a Ni-23 at. % Pt random alloy calculated by the EMTO method using the full charge-density approximation.[32] Other details of the first-principles calculations are as follows.

All the Green's function calculations of the effective chemical interactions were done in the local-density approximation (LDA) using the Perdew-Wang parametrization for the exchange-correlation potential and energy.[39] The partial waves were expanded up to $l_{max}=3$ inside atomic spheres while the multipole moments of the electron density were determined up to $l^{M}_{max}=6$ for the multipole moment correction to the Madelung potential and energy. The Fermi function with $T=925$ K was used during energy integration over the contour. The core states were recalculated after each iteration. Integration over the Brillouin zone has been performed using the Monkhorst-Pack scheme.[40]

In the LDA single-site CPA self-consistent calculations the screened Coulomb interactions were taken into consideration by including the on-site Coulomb screening potential v^{i}_{scr} defined as[30]

$$v^{i}_{\mathrm{scr}} = e^2 \alpha_{\mathrm{scr}} \frac{q_i}{S}, \tag{3}$$

where q_i is the net charge of the atomic sphere of the ith alloy component, S is the Wigner-Seitz radius, and $\alpha_{\mathrm{scr}} \equiv \alpha_{\mathrm{scr}}(\mathbf{R}=0)$ is the on-site screening constant. The on-site screening constant in Ni-25 at. % Pt is 0.74 as has been obtained in the LSGF self-consistent calculations[30] for a 1024-atom supercell modeling a random Ni-25 at. % Pt alloy.

The screening charge was also used to determine the intersite screening constants, $\alpha_{\mathrm{scr}}(\mathbf{R})$, needed in the calculations of the electrostatic part of the SGPM effective pair interactions,[24,30] i.e., the screened intersite Coulomb interactions, which in the case of a binary A-B alloy can be defined as

$$V^{\mathrm{scr}}(\mathbf{R}) = e^2 \alpha_{\mathrm{scr}}(\mathbf{R}) \frac{q^2_{\mathrm{eff}}}{S}, \tag{4}$$

where $q_{\mathrm{eff}}=q_A-q_B$ is the effective charge transfer. The whole SGPM interaction is then

$$V_i \equiv V(\mathbf{R}) = V^{\mathrm{one-el}}(\mathbf{R}) + V^{\mathrm{scr}}(\mathbf{R}), \tag{5}$$

where V_i is the SGPM interaction at the ith coordination shell, given by a set of vectors $\mathbf{R}$, and $V^{\mathrm{one-el}}(\mathbf{R})$ the one-electron contribution to the SGPM interaction.[23,24,30]

The surface energy calculations for the on-site effective cluster interactions, $V^{(1)}_{\lambda}$, were done by employing a semi-infinite geometry with 16 surface and eight vacuum layers for the (110) surfaces. The calculations of the SGPM interactions for the first two surface layers in the case of alloy surfaces were done by the bulk Green's function technique for slabs consisting of 16 atomic and eight vacuum layers.

C. High-temperature magnetism of Ni-25 at. % Pt alloys

Ni-rich Ni-Pt alloys are weak itinerant magnets. The Curie temperature decreases very fast with increasing Pt concentration: from 623 K in pure Ni to about 350 K in Ni-29 at. % Pt alloys.[41] Thus, at the experimental conditions of 923 K, Ni-23.2 at. % Pt is in the paramagnetic state. Unfortunately, there exists quite a serious problem in the first-principles description of such a state in the case of weak itinerant magnets: the time-independent density-functional theory which is used in the usual *ab initio* calculations cannot properly describe the existence of finite local magnetic moments on Ni and Pt atoms: they disappear in the so-called disordered local moment (DLM) calculations which are based on a mean-field model of the paramagnetic state of the system exhibiting a localized type of magnetism.[42] At the same time, the use of more advanced methods, such as, for instance, the dynamical mean-field theory[43] is too cumbersome in this case.

A more practical solution would be the use of a mean-field theory for longitudinal spin fluctuations, similar to that developed in Refs. 44 and 45. In the present work a single-site mean-field approach based on Ref. 45 is used to estimate the average magnetic moment on Ni and Pt atoms in Ni-25 at. % Pt at 925 K. For this purpose the on-site longitudinal spin-fluctuation energy, $E_i(m)$, for each alloy component i was calculated at the lattice spacing of 3.68 Å using constrained LDA calculations with electronic excitations at 925 K included through the Fermi function and electron entropy. The average magnetic moment $\langle m_i \rangle$ was determined using the corresponding partition function assuming that there is full coupling of the transverse and longitudinal degrees of freedom

$$\langle m_i \rangle = \frac{1}{Z_m} \int m^3 \exp[-E_i(m)/k_{\mathrm{B}}T] dm,$$

$$Z_m = \int m^2 \exp[-E_i(m)/k_{\mathrm{B}}T] dm. \tag{6}$$

In this way the averaged magnitudes of the induced magnetic moment of 0.65 and 0.3 for Ni and Pt, respectively, were obtained. It is assumed that they are the same for atoms in the surface region. As demonstrated below, the longitudinal spin fluctuations as well as magnetism itself affect the effective interactions only slightly in this system.

III. EXPERIMENTAL DETAILS

Ingots for crystal growing were produced by arc melting and remelting in an induction furnace, using 99.95 at. %

pure Ni (Praxair MRC, Toulouse, France) and 99.98 at. % pure Pt (Johnson Matthey, London, United Kingdom).

A single crystal with a diameter of 12 mm was grown by use of the Bridgman technique in an Al_2O_3 crucible. A slice with a ⟨110⟩ surface normal, 11.5 mm in diameter and 3.5 mm in thickness, was cut by spark erosion. Its composition, determined by x-ray fluorescence analysis using standards, was Ni-23.2(3) at. % Pt. The sample was homogenized under Ar at 1373 K for 69 h and quenched into ice brine. It was mechanically polished (finally with silica sol being 0.04 μm in grain size) employing a Logitech PM5 Autolap lapping/polishing system. The deviation from a ⟨110⟩ surface normal was about 0.02°. The sample was mounted in a portable UHV chamber used in the scattering experiment. Sputtering at 670 K with Ar^+ ions of 0.8 keV energy and annealing at 900 K were repeatedly applied. A high annealing temperature was selected also to reduce preferential sputtering of Ni atoms through thermal equilibration by diffusion.[8]

The diffuse scattering intensity was recorded at the (2 +3) surface diffractometer of the Materials Science Beamline (SLS, Villigen PSI, Switzerland).[46] Data were taken at 923 K with an incoming photon energy of 9800 eV at an angle of incidence α_i=0.30° (the critical angle of total reflection is α_c=0.39°). Intensity was registered at about 650 in-plane positions within 0.28 to 3.1 rlu (with an angle of exit of 0.30°) and 250 out-of-plane positions located on planes shifted by (−0.45,0.45,0) and (−1,1,0), respectively. Exploiting the vertical opening angle of the Pilatus II 2D pixel detector, additional data could be read out for every position displaced by at most (−0.07,0.07,0). Typical intensities were 500–5000 counts per 200 s. The mosaicity of the near-surface microstructure amounted to 0.1° full width at half maximum.

A. Diffuse scattering theory

The elastic diffuse scattering I_{diff} from crystalline solid solutions is due to the presence of different types of atoms that are not strictly periodically arranged on a lattice (short-range order scattering I_{SRO}) and to the static local deviations of the atoms from the sites of the average lattice (displacement scattering). The latter scattering contribution is usually approximated by size-effect scattering I_{SE} and Huang scattering I_{H} (see, e.g., Ref. 12 and references therein). For a cubic binary *A*-*B* alloy the diffuse scattering intensity per atom is given by

$$I_{\mathrm{diff}}(\mathbf{h})/N = c_A c_B |f_A - f_B|^2 [I_{\mathrm{SRO}}(\mathbf{h}) + I_{\mathrm{SE}}(\mathbf{h}) + I_{\mathrm{H}}(\mathbf{h})] \quad (7)$$

with

$$I_{\mathrm{SRO}}(\mathbf{h}) = \sum_{lmn} \alpha_{lmn} \cos(\pi h_1 l)\cos(\pi h_2 m)\cos(\pi h_3 n), \quad (8)$$

$$I_{\mathrm{SE}}(\mathbf{h}) = \sum_i h_i Q_i(\mathbf{h}) \quad (9)$$

and, e.g.,

$$Q_x(\mathbf{h}) = \sum_{lmn} \gamma^x_{lmn} \sin(\pi h_1 l)\cos(\pi h_2 m)\cos(\pi h_3 n). \quad (10)$$

Here, c_μ is the atomic fraction of the component $\mu = A, B$ and f_μ is the atomic scattering factor. The prefactor in Eq. (7), $c_A c_B |f_A - f_B|^2$, is called one Laue unit (Lu). The scattering vector $\mathbf{h}=(h_1,h_2,h_3)$ is given in reciprocal lattice units $2\pi/a$ (rlu, a=lattice parameter). The quantities of interest are the Fourier coefficients of the corresponding Fourier series. In the case of short-range order scattering, these are the Warren-Cowley short-range order parameters α_{lmn} for the *lmn* type of neighbors (l,m,n in units of $a/2$).[47] In the case of size-effect scattering, the coefficients γ^x_{lmn} represent linear combinations of the species-dependent static atomic displacements.

For a statistically uncorrelated arrangement of atoms on a lattice, all α_{lmn} are zero, except for α_{000} which is unity. The sign of the nearest neighbor α_{lmn} is usually taken to distinguish systems that tend to local order or local decomposition.

To separate the various scattering contributions, the leading Fourier coefficients were least-squares fitted, an appropriate procedure if scattering is weakly modulated.

B. Intensity analysis

Data were corrected for background, the variation in the active sample area with changing scattering vector, polarization (here complete linear polarization within the horizontal scattering plane was assumed). They were treated within the distorted-wave Born approximation.[48] For the combined effect of detector heterogeneity and intensity transmittivity, data from a separate measurement that mainly comprises Ni K fluorescence, was employed.

To calculate thermal diffuse scattering (TDS), elastic constants c_{ij} were determined at room temperature for a separate single-crystalline piece with the pulse-echo-overlap method. Using the temperature dependence of the c_{ij} of pure Ni (from Ref. 49), the elastic constants of Ni-23.2 at. % Pt were estimated to c_{11}=231(2) GPa, c_{12}=173(2) GPa, and c_{44} =103(1) GPa at 923 K. With these values and the lattice parameter change with composition, $a^{-1}da/dc$=0.12, a value of $B=1.41\times10^{-2}$ nm^2 was obtained for the total (static and dynamic) Debye-Waller factor $\exp[-B(h/2a)^2]$ in the bulk at 923 K.

To calibrate diffuse scattering, the intensity close to Bragg reflections (within 0.25 rlu) was employed, where thermal diffuse scattering and Huang scattering are dominant for a locally ordered alloy. A separate investigation on an in-house four-circle diffractometer using MoKα radiation was performed and the ratio between the measured intensity (calibrated with polystyrene) and TDS was determined to be about 2.5 at room temperature. Employing the temperature dependence of the elastic constants and of the B value (0.49×10^{-2} nm^2 at room temperature), this ratio changes to about 1.6 at 923 K.

To obtain the elastic diffuse scattering, the calculated thermal diffuse scattering up to third order and Compton scattering[50] were subtracted. Atomic scattering factors and Hönl corrections were taken from Refs. 51 and 52.

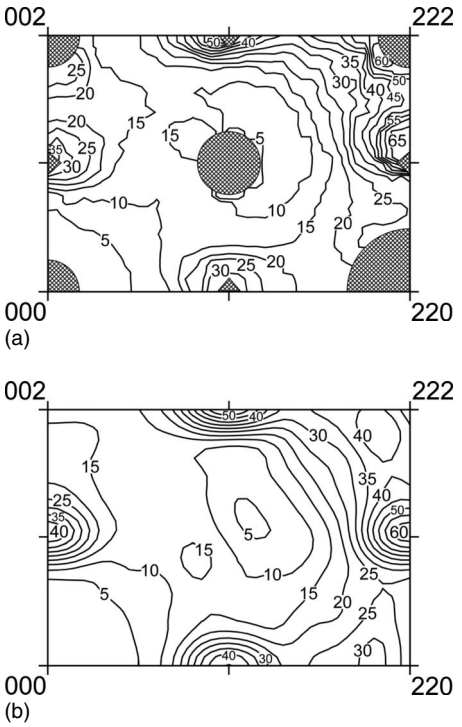

FIG. 1. Elastic diffuse scattering from Ni-23.2 at. % Pt(110) in 0.1 Lu, taken under an angle of incidence and exit of 0.3°. The area close to Bragg reflections, the direct beam and the crystal truncation rods is marked in the experimental data (a). Diffuse scattering was recalculated using the fitted parameters of Tables I and III (b).

IV. EXPERIMENTAL RESULTS

The elastic diffuse in-plane scattering is given in Fig. 1, an example of out-of-plane scattering is shown in Fig. 2. Diffuse maxima much broader than the scattering from the crystal truncation rods, are visible at positions of the X type. The general increase in intensity for larger scattering angles stems from the increasing contribution of static atomic-displacement scattering. There is also an asymmetry in diffuse scattering around the diffuse maxima and an increase toward Bragg reflections because of size-effect scattering and Huang scattering, respectively.

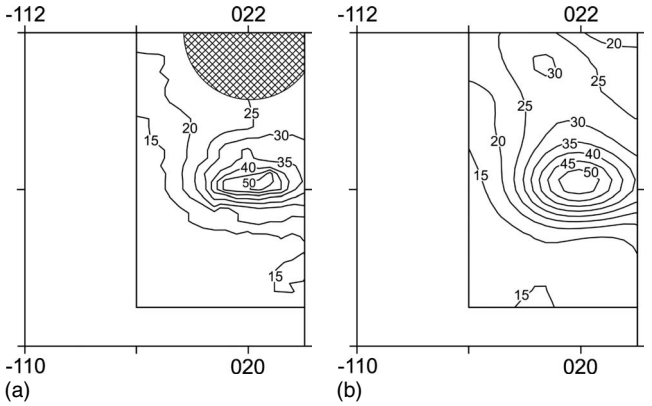

FIG. 2. Elastic diffuse scattering from Ni-23.2 at.% Pt(110) in 0.1 Lu, taken under an angle of incidence of 0.3°. The out-of-plane scattering refers to a plane shifted by $(-1,1,0)$ (a). Diffuse scattering was recalculated using the fitted parameters of Tables I and III (b).

Data were transferred to Laue units (this presents a global unit as the average composition of the sample was employed) using $B=2.0\times10^{-2}$ nm^2 for the total Debye-Waller factor. A calibration factor of 2.5, comparable to the range of 1.6–2.5 estimated on the basis of the elastic constants, was required to reach a value of α_{000} close to the theoretical value of 1 in the subsequent least-squares fitting to the leading Fourier coefficients. Variation in B between the estimated bulk value of 1.4×10^{-2} nm^2 and an assumed increase up to 3×10^{-2} nm^2 for the near-surface microstructure modified the values of the α_{lmn} and γ^x_{lmn} just within one standard deviation while the Fourier coefficient δ^x_{000} of Huang scattering varied by seven standard deviations. A larger number of Fourier coefficients of quadratic displacement scattering could be neglected as the range of data not considered in the least-squares fitting, was set to 0.4 rlu around Bragg positions.

A. Cubic isotropic site occupation

A set of 16 α_{lmn}, 12 γ^x_{lmn}, and 1 Fourier coefficient of quadratic displacement scattering was employed. The quality in the fit was $R=0.14$. The recalculated diffuse in-plane and out-of-plane scattering is also given in Figs. 1 and 2.

The Warren-Cowley short-range order parameters are summarized in Table I. The sign sequence of the α_{lmn} follows that of the $L1_2$ superstructure with α_{110} reaching 45% of its maximum value at the given composition. Short-range order scattering recalculated with the α_{lmn} of Table I for the (100) plane is shown in Fig. 3. A disk-shaped pattern of isointensity lines around the diffuse maxima (about 4 Lu) is most striking, a feature that is usually connected with local elements of antiphase regions (Ref. 53, see also the discussion of Clapp configurations below).

As model crystals, films with a $\langle110\rangle$ normal, 64×64 in cross section and just 32 layers in thickness, were used. This thickness corresponds to about twice the length over which the z component of the evanescent wave decays to $1/e$. Periodic boundary conditions were only applied parallel to the surface while the top and bottom surfaces were kept free. Crystals were modeled incorporating or neglecting a segregation profile at both free surfaces. For the segregation profile, a top layer of Ni-0 at. % Pt and a second layer of Ni-60 at. % Pt were used while the other layers had bulk composition (see Gauthier,[1] the data are based on LEED investigations and might differ from those valid at 923 K). The α_{lmn} of model crystals with a segregation profile had a slightly lower quality in fitting than those without a segregation profile. However, the α_{lmn} of all model crystals were always within 0.1 standard deviations.

The abundance of Clapp configurations[54] does not differ much among the two crystal types considered. Subsequently, data were taken from those with a segregation profile. In Table II, the Clapp configurations most enhanced with respect to a statistically uncorrelated arrangement of the same composition, are summarized. They are given for the case of Pt atoms around a Ni atom, as this case is best suited to

TABLE I. Warren-Cowley short-range order parameters α_{lmn} for Ni-23.2 at. % Pt at 925 K: experiment (this work) and theory (Monte Carlo simulations using first-principles effective interactions for bulk microstructure, see text for details). In comparison, the parameters for Ni_3Pt with $L1_2$ are given.

		α_{lmn} theory			
lmn	α_{lmn} experiment	$V^{(2-4)}$	$V^{(2)}$	$V^{(2)}_{1-7}$	$L1_2$
000	0.9943(235)	1.000	1.000	1.000	1.000
110	−0.1359(48)	−0.166	−0.161	−0.161	−0.333
200	0.1660(46)	0.170	0.165	0.164	0.333
211	0.0021(30)	0.038	0.033	0.034	−0.333
220	0.0519(36)	0.042	0.047	0.046	0.333
310	−0.0408(23)	−0.062	−0.058	−0.058	−0.333
222	0.0066(40)	−0.027	−0.014	−0.020	0.333
321	−0.0059(17)	−0.004	−0.006	−0.006	−0.333
400	0.0348(41)	0.055	0.051	0.053	0.333
330	−0.0126(30)	−0.016	−0.018	−0.016	−0.333
411	0.0065(23)	0.026	0.025	0.023	−0.333
420	0.0081(21)	0.016	0.016	0.018	0.333
233	0.0010(24)	0.008	0.006	0.007	−0.333
422	0.0002(23)	−0.007	−0.004	−0.004	0.333
431	0.0027(16)	0.002	0.003	0.001	−0.333
510	−0.0107(23)	−0.026	−0.024	−0.024	−0.333

consider elements of the $L1_2$ structure: the building elements of the $L1_2$ structure and an antiphase region within such an $L1_2$ structure are C16 and C17, respectively. The seven configurations listed may be grouped into one related to $L1_2$ (with more or less Pt atoms than for C16: C34, C7, and C59) and another similarly related to C17 (C35). C18 is related to both groups. With 24% these seven configurations comprise a major fraction of all Clapp configurations.

Concerning fingerprints of other superstructures, one might envisage $L1_0$ known for bulk Ni-Pt. As the characteristic feature for the case of Pt atoms around a Ni atom is C16 for both superstructures, one now considers the case of Pt atoms around a Pt atom, where the configurations are C1 and C16 for $L1_2$ and $L1_0$, respectively. Both are the most enhanced configurations, C16 with 3.2 (0.5%) and C1 with 3.7 (17%), with totally different abundances (numbers in brackets).

Species-dependent static atomic displacements are not accessible from the present data, only the linear combinations γ^x_{lmn}. The data of the first six shells are given in Table III. Comparing them with those from an earlier x-ray investigation of Ni-87.8 at. % Pt (Ref. 18), they are found similar in magnitude. This is surprising as relaxation is known for the (110) surface: a Ni-10 at. % Pt(110) showed variation in the top interlayer spacings by several percentages from the bulk interlayer spacing.[4] A bulk x-ray measurement with the same composition is indicated to highlight the relaxation effects due to the surface.

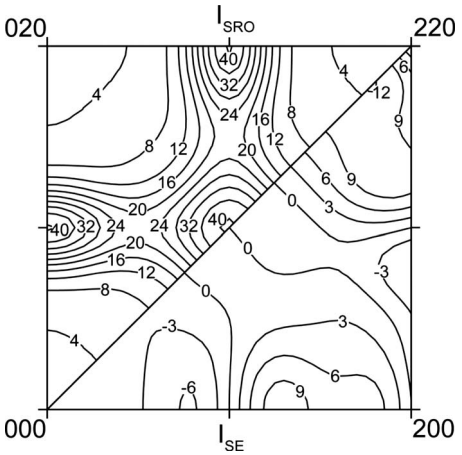

FIG. 3. Recalculated short-range order scattering and size-effect scattering in 0.1 Lu for the $h_1,h_2,0$ plane.

TABLE II. Abundance analysis of nearest-neighbor configurations (Clapp configurations) with largest enhancement factors for the short-range ordered state. The case of Pt atoms around any Ni atom is considered. The nomenclature of the sites refers to Clapp (Ref. 54).

Clapp configuration	Sites occupied	Enhancement factor	Abundance in %
C16	5,6,7,8	29.8	3.2
C59	2,4,5,6,9,11	16.8	0.3
C17	4,6,7,9	12.1	2.6
C34	5,6,7,8,11	9.8	2.4
C35	4,6,7,9,11	5.3	1.5
C7	5,6,7	5.1	7.1
C18	5,6,8,11	4.6	7.0

TABLE III. Fitted parameters γ^x_{lmn} of size-effect scattering.

lmn	γ^x_{lmn}
110	−0.0742(22)
200	0.0059(44)
211	0.0177(24)
121	−0.0031(16)
220	0.0194(22)
310	−0.0142(23)
130	−0.0082(19)
222	0.0026(23)

B. Tetragonal anisotropic site occupation

The same set of scattering intensities was also fitted based on a microstructure that shows a tetragonal site occupation. A noncubic site occupation is present as there is a segregation profile.

To limit the number of Fourier coefficients, tetragonally averaged values were employed together with the following further simplifications. (i) The neighbors in any shell are sorted with respect to the orientation of their distance vector and the surface normal; those atoms with connecting lines closest to the surface normal are labeled as parallel, those furthest away as perpendicular, while the rest is called inbetween. This yields at most three Warren-Cowley short-range order parameters and nine displacement parameters per shell. (ii) Also α_{000} was set to 1 and not fitted to limit the number of free parameters.

A set of 11 α_{lmn}, 11 γ^x_{lmn}, and 1 Fourier coefficient of quadratic displacement scattering was employed, the quality of the fit was $R=0.29$ (Table IV). This value is higher than for the cubic fit (Table I), as the number of Fourier coefficients has to be kept small. The α_{lmn} of Table IV may be compared with those for an alternating stacking of (110) planes consisting only of Ni and Pt atoms, respectively—this is equivalent to the $L1_0$ structure of NiPt. A large difference exists for the nearest-neighbor case with α_{110} being 1 for the parallel and perpendicular case of Table IV and −1 for the inbetween case. These values much differ from −1/3 for the $L1_2$ structure (Table I). It may be concluded that the presence of the segregation profile suppresses the tendency toward $L1_2$ for the direction perpendicular to the segregation profile. A determination of α_{110} for the bulk microstructure will be helpful—such a measurement is currently under way.

For the nearest-neighbor displacement parameters there is also a large difference with γ^x_{110} being distinctly larger for parallel [with −0.172(34)] than for perpendicular [with −0.065(6)] or inbetween [with −0.072(4)]. This might be expected, still species-dependent parameters will be required for further conclusions.

C. Ordering energy

EPI parameters were determined using the inverse Monte Carlo (IMC) method[55] as well as the Krivoglaz-Clapp-Moss (KCM) approximation[56,57] with the corrections from the γ-expansion method (GEM) (Ref. 58). The EPI parameters in dependence of the shell indices l,m,n of an A-B alloy, $V_{lmn}=V^{AA}_{lmn}+V^{BB}_{lmn}-2V^{AB}_{lmn}$, are connected with the ordering energy per atom, E_{ord}, defined by

$$E_{\mathrm{ord}} = \frac{1}{2} c_A c_B \sum_{lmn} V_{lmn} \alpha_{lmn}. \tag{11}$$

In Table V the EPI parameters are listed. They were determined with linear boundary conditions for the IMC method. A set of eight parameters was sufficient considering the standard deviations that were obtained on the basis of the standard deviations of the α_{lmn} of Table I. Employing this set of EPI parameters in subsequent Monte Carlo simulations, the recalculated short-range order scattering showed 100 maxima higher than those recalculated from the α_{lmn} of Table I; they amount to 6.2 instead of 4.1 Laue units. This is not unexpected for the situation close to an order-disorder transition temperature. In fact, Monte Carlo simulations yield a value of 865(10) K for stoichiometric Ni-25 at. % Pt and a slightly lower value of 835(10) K for the present composition of Ni-23.2 at. % Pt. In both cases the starting model crystals had a maximum degree of $L1_2$-type long-range order. Both values for the transition temperature are close to 853 K, the known transition temperature for the bulk microstructure.[59]

The EPI parameters were also determined by use of the KCM-GEM method. The data are given in Table V. They are

TABLE IV. Fitted Warren-Cowley short-range order parameters α_{lmn} for Ni-23.2 at. % Pt using a tetragonal site occupation. In comparison, the parameters recalculated from the layer-resolved parameters of the top ten layers (Table IX) are given. Neighboring atoms are sorted with respect to the angle between surface normal and the connecting vectors; as parallel (par) and perpendicular (per) if the connecting line is closest or furthest away from the surface normal, otherwise the neighboring atoms are called inbetween (inb).

	α_{lmn} experiment			α_{lmn} (Table IX)		
lmn	par	per	inb	par	per	inb
000		1			1	
110	−0.116(9)	−0.211(12)	−0.150(19)	−0.137	−0.122	−0.126
200	0.195(6)	0.192(10)		0.117	0.101	
211	0.045(20)	0.038(8)	−0.013(4)	0.032	0.031	0.029
220	0.017(15)	0.063(9)	0.059(3)	0.031	0.031	0.029

TABLE V. EPI parameters V_{lmn} as determined from the set of α_{lmn} of Table I. The IMC method as well as the Krivoglaz-Clapp-Moss high-temperature approximation including the corrections by the γ-expansion method (KCM-GEM) were used. In comparison, the results from Ni-48 at. % Pt (Ref. 17) and Ni-87.8 at. % Pt (Ref. 18) are given. In comparison with Refs. 17 and 18 data were multiplied by 2 to stay consistent with Eq. (11).

	V_{lmn} (Ni-23.2 at. % Pt) (meV)		V_{lmn} (Ni-48 at. % Pt) (meV)	V_{lmn} (Ni-87.8 at. % Pt) (meV)
lmn	IMC	KCM-GEM	KCM-GEM	IMC
110	85.4(24)	87.6(18)	53.2(24)	24.4(8)
200	−28.6(26)	−29.6(16)	−10.6(18)	−16.6(4)
211	0.2(12)	5.2(14)	3.0(20)	11.8(6)
220	−0.2(14)	4.4(14)	−7.0(0)	−9.2(2)
310	1.0(10)	6.2(18)	−1.6(26)	−1.2(4)
222	3.8(26)	6.6(6)	−0.6(18)	4.6(2)
321	0.8(6)	4.6(16)	0.2(20)	−1.2(2)
400	−0.4(14)	−7.0(12)	5.4(24)	−0.4(4)

expected to be of lower quality than those from IMC simulations as the prerequisite of a high-temperature approximation is no longer fulfilled close to the order-disorder transition temperature. Still, a generally good agreement is seen.

In comparison, the EPI parameters from diffuse scattering experiments of other Ni-Pt alloys are provided. Two points are to be noted. (i) The nearest-neighbor EPI parameter increases with increasing Ni fraction. Such an increase was predicted by Paudyal *et al.*[60] although their calculations were restricted to bulk microstructures. (ii) The ordering energy for Ni_3Pt ($L1_2$) amounts to −47.8 meV, lower than for $NiPt_3$ ($L1_2$) with about −35 meV (see Ref. 18). This is consistent with the finding that Ni_3Pt with $L1_2$ is well known experimentally while indications for $NiPt_3$ with $L1_2$ were only recently noted following a thermal treatment where quenched-in vacancies were provided prior to aging at temperatures below 650 K.[18]

V. FIRST-PRINCIPLES RESULTS

A. On-site interactions (surface segregation energies)

On-site effective interactions of Hamiltonian (1) are in fact the surface segregation energies of an equiatomic homogeneous random alloy (half in value due to the use of spin variables). Within the KKR-ASA method these energies have already been obtained in Ref. 22 but for the lattice parameter of bulk Ni-50 at. % Pt. They have been recalculated for the lattice spacing of 3.68 Å taking into consideration one-electron thermal excitation at 925 K through the Fermi function. The values of the on-site interactions are given in Table VI. For comparison the values obtained for Ni-50 at. % Pt in Ref. 22 are also given. One can see that they are very close to each other with a negative shift of the surface segregation energy (for Pt) in the present case. This shift is consistent with the strong decrease in the (110) surface energy of Pt with decreasing lattice spacing (see Table III of Ref. 22).

The major drawback of these calculations is the unaccounted contribution from local lattice relaxations. In order to estimate this contribution, FP-PAW slab-supercell calculations of the surface segregation energy of Pt on the (110) surface of Ni were performed. First, GGA ferromagnetic calculations of the pure Ni(110) surface were done. Although the GGA produces quite a substantial error for the surface energy compared with the LDA, it produces more accurately the ground-state properties of the 3*d* metals, and one can get a better description of the relaxation geometry for the Ni(110) surface. The supercell comprised 14 atomic layers separated by about three lattice spacings. A substantial relaxation of interlayer spacing for the (110) surface of Ni was found: the first two layers are contracted toward each other by 10.4% while the interlayer spacing between the second and third layers increases by 3.4%. The relaxation energy for the pure Ni(110) surface is about 0.04 eV per surface atom.

Next, the segregation energy of Pt for the first two layers was determined by putting a Pt atom into these layers and into the seventh layer, which is supposed to represent the bulk in this case. For each case total-energy calculations were done allowing for local lattice relaxations of all the atoms. The supercell for these calculations comprised 14 atomic layers separated by about three lattice spacings and consisted of 168 atoms ($4\times3\times14$). The segregation energies of Pt in the first and second layer are then −0.298 and −0.321 eV. The LDA nonmagnetic values of the segregation

TABLE VI. Effective on-site interactions of the surface Hamiltonian obtained in first-principles calculations.

	$V_\lambda^{(1)}$ (meV)			
λ=	1	2	3	4
Ni-23 at. % Pt (this work)	−20.5	−103.4	−23.7	16.9
Ni-50 at. % Pt (Ref. 22)	14.4	−76.0	−22.8	14.0

TABLE VII. Chemical part of the EPI parameters $V_{lmn}^{(2)}$ obtained in the first-principles calculations. The values for Ni-23 at. % Pt in parentheses are the total EPIs, which include the strain-induced interactions.

	V_{lmn} Ni-25 at. % Pt (meV)			V_{lmn} Ni-23 at. % Pt (meV)	V_{lmn} Ni-50 at. % Pt (meV)	V_{lmn} Ni-75 at. % Pt (meV)
lmn	FM	NM	DLM	DLM	DLM	
110	240.27	240.46	238.38	237.26(116.57)	255.87	278.85
200	19.71	4.88	7.82	8.08(−12.46)	4.92	2.80
211	−12.01	−17.88	−15.54	−15.62(−12.63)	−14.23	−11.78
220	−18.39	−22.03	−20.54	−20.25(−10.72)	−24.86	−30.12
310	2.35	1.31	1.41	1.40	1.75	2.08
222	5.90	4.87	4.88	4.85	5.47	6.29
321	1.63	1.50	1.54	1.54	1.51	1.64
400	−0.50	0.12	−0.01	−0.01	0.05	0.32
411	−0.01	−0.11	−0.08	−0.08	−0.07	−0.01
330	−0.10	0.64	0.15	0.03	−0.52	−2.22
422	0.42	−0.23	−0.04	−0.05	−0.04	−0.05
431	−0.29	−0.23	−0.22	−0.20	−0.42	−0.75
440	0.41	0.87	0.63	0.60	1.07	1.61

energies were then calculated using the geometry from the GGA ferromagnetic calculations in order to better adapt to the real experimental geometry. The resulting values are −0.055 and −0.329 eV for the first and second layer. Both results agree in one important point: the segregation of Pt in the second layer is more preferable than in the first. This is in accord with the surface segregation energies from Green's function calculations.

B. Effective cluster interactions

1. Chemical part

The chemical part of the effective cluster interactions were obtained by the SGPM method[23,24] for the lattice spacing of 3.68 Å by use of the KKR-ASA and EMTO method. Here the EMTO results are presented, which are supposed to be more accurate (particularly owing to the correct spatial normalization of the electron density) although both methods produce practically the same results. In Table VII bulk effective pair interactions obtained in three different magnetic states are presented: nonmagnetic (NM), ferromagnetic (FM), and paramagnetic (DLM) for Ni-25 at. % Pt. One notices that the EPIs are not much affected by the magnetic state. This especially concerns the difference between the effective pair interactions in the nonmagnetic and paramagnetic (DLM) states. The interactions are relatively short ranged. The rest of the EPIs are less than 0.14 meV.

In this table the EPIs for three other alloy compositions are also shown that were obtained for the same (DLM) magnetic state and lattice spacing (3.68 Å). One can see that the concentration dependence of the EPIs is weak. In real alloys it is, however, quite strong (see Table V), which is clear when comparing ordering in the cases of Ni-25 at. % Pt and Ni-75 at. % Pt. While it is quite pronounced in the first case, it is rather weak in the second. This is in fact opposite to the concentration dependence of the EPIs in Table VII. The reason for such a dramatic weakening of the ordering in the case of Pt-rich alloys is the very strong volume dependence of the EPI parameters: with increasing lattice spacing (which follows the increasing Pt fraction in the alloy) the electrostatic contribution (from the screened Coulomb interactions) to the nearest-neighbor EPI, which is dominant, decreases with the volume, thereby reducing the ordering effect. For instance, the nearest-neighbor EPI in Ni-25 at. % Pt, which contains the greatest contribution from the screened Coulomb interactions, drops down from 389 meV for the lattice spacing of Ni to 108 meV for the lattice constant of Pt. This is very similar to the situation in Cu-Au described in Ref. 24.

The strongest three-site interactions are for the triangle of nearest neighbors and for the cluster formed by the three successive sites in the closed packed direction, which both are approximately equal to 6.7 meV in the paramagnetic state and 7.3 and 8.6 meV, respectively, in the ferromagnetic one. The strongest four-site interaction is for the cluster formed by the four successive sites in the closed packed direction. It is about 2.7 meV in the paramagnetic state. The contribution of the multisite interactions to, for instance, the ordering energy of the $L1_2$ structure is only about 2.7 meV while the ordering energy (chemical part only, i.e., without contribution from local lattice relaxations in the random alloy) is 95 meV. This result is in good agreement with the direct total-energy calculations of the $L1_2$ ordering energy of 91 meV, which was obtained for a fixed ideal fcc lattice (no local lattice relaxations in the random alloy) and the same paramagnetic state. Inclusion of the multisite interactions into the Monte Carlo simulations increases the order-disorder transition temperature only by about 20 K. Therefore, multisite interactions were neglected in the surface Monte Carlo calculations.

The effective chemical interactions are not much affected by the surface, which has also been found for

Ni-50 at. % Pt(110) in Ref. 22. The largest renormalization of the interactions is found for the nearest-neighbor ones in the surface plane: it is reduced by about 54 meV. The renormalization of other interactions is relatively small, similar to that found in Ref. 22. Note that the interactions presented in Ref. 22 are factorized by the corresponding number of the interactions of a given type. This allows one to easily see the resulting effect leading to the strong nearest-neighbor interlayer ordering in the case of the (110) surface compared with the intralayer ordering and ordering between second nearest-neighbor layers.

2. Strain-induced interactions

Strain-induced interactions at the first four coordination shells for the bulk alloy were obtained in the dilute limit of Pt in Ni in the FP-PAW calculations in the ferromagnetic state for the lattice spacing of 3.68 Å in the GGA as described in Ref. 18

$$V_{\mathrm{si}}(\mathbf{R}) = \Delta E_{\mathrm{rel}}^{\mathrm{Pt-Pt}}(\mathbf{R}) - 2\Delta E_{\mathrm{rel}}^{\mathrm{Pt}}. \tag{12}$$

Here, $\Delta E_{\mathrm{rel}}^{\mathrm{Pt-Pt}}$ and $\Delta E_{\mathrm{rel}}^{\mathrm{Pt}}$ are the local relaxation energies of a Pt pair at the corresponding coordination shell $\mathbf{R}$ and a single Pt atom, respectively, in Ni (the volume and the geometry of the supercell are kept fixed). As in Ref. 18, 256-atom supercells were used ($4\times4\times4$ supercells, built on four-atom fcc cells) consisting of a Pt pair in Ni and a single Pt atom, respectively.

The values obtained are −120.7, −20.5, 3.0, and 9.7 meV for the first to the fourth coordination shell. They were added to the chemical part of the EPIs in both surface and bulk Monte Carlo simulations. As one can see in Table VII, they give substantial contributions to the total EPIs at the first two coordination shells. Including strain-induced interactions the ordering energy is then reduced to −49.3 meV, which is in very good agreement with the value of −47.8 meV (see Sec. IV C) from experimentally evaluated EPIs. Note that in spite of such agreement between the theoretical and experimental estimate of the ordering energy, the EPIs employed are quite different, which is clear if one compares the total interactions given in parentheses in Table VII and the interactions in Table V. The origin of the differences is unknown and additional investigation is required. As shown below, the first-principles interaction parameters still reproduce reasonably well the Warren-Cowley short-range order parameters from experiment.

Although the strain-induced interactions near the surface can be substantially different from these bulk values, as will be shown below, this fact is not important owing to the very strong segregation of Ni atoms in the surface layer which eliminates the contribution to the ordering energy from the surface layer. The long-range tail of the strain-induced interactions was ignored in this study.

The EPI parameters of Tables V and VII do not show such a close agreement as previously achieved on the Pt-rich side of Ni-Pt alloys (see Tables V and VI of Ref. 18). Again, the strain-induced interactions are important especially for the nearest neighbors. As shown below, a close agreement is still observed in the order-disorder transition temperature of Ni-25 at. % Pt using the various sets of EPIs in Monte Carlo simulations; always values close to 853 K, the value known for the bulk microstructure, were obtained.

C. Concentration profile and atomic distribution functions from *ab initio* effective interactions

Bulk Monte Carlo simulations based on the Metropolis algorithm were performed with different sets of effective interactions for 25 at. % Pt using a simulation box containing 16 384 atoms ($16\times16\times16$ of four-atom fcc unit cells). If the whole set of interactions is used, i.e., effective pair interactions up to the 30th coordination shell and the strongest three- and four-site interactions, the order-disorder transition temperature is about 840 K, which is in excellent agreement with the experimental value of 853 K. If only effective pair interactions are included, the transition temperature is about 820 K. This result is practically unchanged if only the first seven effective pair interactions are used. For Ni-23 at. % Pt the order-disorder transition temperature is about 800 K when using the whole set of interactions.

The calculated Warren-Cowley short-range order parameters for Ni-23 at. % Pt at 925 K are presented in Table I. The column, designated as $V^{(2-4)}$, shows the results when the total effective pair interactions (chemical plus strain induced) up to the 30th coordination shell and some of the strongest three- and four-site interactions are included. In the next column, designated as $V^{(2)}$, the results with only 30 effective pair interactions are shown. As one can see the multisite interactions play a minor role in this system and therefore they will be neglected in the surface Monte Carlo simulations. And finally in column $V_{1-7}^{(2)}$ the short-range order parameters calculated with inclusion of only the first seven effective pair interactions are given. One can see that the first seven EPIs reproduce almost exactly the short-range order parameters in Table I that were obtained with 30 EPIs.

A general agreement is observed in sign and magnitude between the calculated and the experimental Warren-Cowley short-range order parameters in Table I. The slight variation is taken as an indication that the differences between the bulk (for which the theory data stand) and the near-surface microstructure are small and high-quality data together with the presence of a long-range segregation profile are required to state a difference in microstructure beyond any doubt.

In the case of alloy surfaces, the direct exchange Monte Carlo method[22] was used. This is a grand-canonical ensemble technique simulating the exchange of atoms between the bulk and the surface region. The size of the simulation box for surface calculations was 24×24 in the planes parallel to the surface and 24 layers in thickness. The calculated surface segregation profile is presented in Table VIII. The surface layer and the third layer mostly consist of Ni atoms while the Pt fraction in the second layer reaches 75 at. %. This result is in good agreement with experimental data.[1] Note that the mechanism of the Ni enrichment of the surface layer is exactly the one for the segregation reversal described in Refs. 20 and 22, i.e., Pt segregation in the second layer and a strong interlayer ordering due to the interactions at the first coordination shell.

To characterize ordering in inhomogeneous systems, one can use layer-resolved short-range order parameters, defined as

TABLE VIII. Pt composition near the (110) surface of Ni-23 at. % Pt alloy at 925 K: Monte Carlo simulation results with *ab initio* interactions.

Layer	1	2	3	4	5	6	7	8
at. % Pt	0.01	0.75	0.08	0.14	0.35	0.15	0.27	0.22

$$\alpha_p^{\lambda,\lambda'} = 1 - \frac{\langle c_\lambda(0)[1 - c_{\lambda'}(\mathbf{R})]\rangle}{c_\lambda(1 - c_{\lambda'})}, \tag{13}$$

where the lattice vector **R** belongs to the pth coordination shell between layers λ and λ'.

In Table IX we show $\alpha_p^{\lambda,\lambda'}$ for the first four shells of the fcc lattice and the first ten layers. Very small SRO parameters are seen in the first and third layer, as well as for the corresponding interlayer SRO, due to the fact that they practically do not contain any Pt atoms. One can also see that surface segregation substantially affects short-range order in at least seven to eight layers near the surface.

The layer-dependent short-range order parameters of Table IX were converted to α_{lmn} as accessible from diffuse scattering and presented in Table IV in the following way; they were weighted over the first ten layers according to the exponentially decaying evanescent wave. The agreement seen in Table IV mainly refers to the general strength of the parameters. A much larger number of registered scattering

TABLE IX. Layer-resolved short-range order parameters near the (110) surface of Ni-23 at. % Pt alloy, $\alpha_p^{\lambda,\lambda'}$, obtained in Monte Carlo simulations using *ab initio* effective interactions. Here, $p(lmn)$ refers to the fcc bulklike coordination shells.

$p(lmn)=110$			200		211				220		
$\lambda'=\lambda$	$\lambda+1$	$\lambda+2$	λ	$\lambda+3$	λ	$\lambda+1$	$\lambda+2$	$\lambda+3$	λ	$\lambda+2$	$\lambda+4$
					$\lambda=1$						
−0.002	−0.050	−0.001	0.010	0.018	0.002	0.010	0.026	0.011	−0.001	0.008	−0.004
					$\lambda=2$						
−0.171	−0.140	−0.230	0.043	0.101	0.053	0.036	0.010	0.054	0.050	0.010	0.020
					$\lambda=3$						
−0.046	−0.068	−0.132	0.093	0.091	0.035	−0.007	0.008	0.021	0.004	0.021	0.053
					$\lambda=4$						
−0.110	−0.158	−0.070	0.099	0.101	0.026	0.064	0.067	0.031	0.017	0.031	0.001
					$\lambda=5$						
−0.239	−0.155	−0.245	0.132	0.202	0.028	0.038	0.020	0.042	0.070	0.038	0.078
					$\lambda=6$						
−0.088	−0.139	−0.114	0.160	0.123	0.043	0.014	0.036	0.025	0.013	0.042	0.032
					$\lambda=7$						
−0.210	−0.169	−0.179	0.140	0.180	0.029	0.056	0.041	0.036	0.073	0.041	0.052
					$\lambda=8$						
−0.142	−0.156	−0.157	0.173	0.156	0.033	0.024	0.029	0.034	0.022	0.046	0.042
					$\lambda=9$						
−0.169	−0.161	−0.162	0.154	0.165	0.043	0.036	0.038	0.034	0.056	0.043	0.042
					$\lambda=10$						
−0.161	−0.160	−0.163	0.163	0.164	0.032	0.032	0.031	0.035	0.044	0.048	0.046
					Bulk, average						
−0.161	−0.161	−0.161	0.164	0.164	0.034	0.034	0.034	0.034	0.046	0.046	0.046
					Bulk, $L1_2$ ordered						
					$\lambda=1$						
0.0	0.0	0.0	0.0	0.0	0.0	0.0	0.0	0.0	0.0	0.0	0.0
					$\lambda=2$						
−1.0	0.0	−1.0	−1.0	1.0	1.0	0.0	1.0	0.0	1.0	−1.0	1.0

intensities is required to allow for more α_{lmn} to be fitted and an R value to be obtained, that is, at least as good as for a cubic site occupation.

VI. DISCUSSION

In this investigation, a 3D microstructural analysis was performed on the basis of out-of-plane scattering in addition to in-plane scattering. The strategy to explore larger and larger volumes in reciprocal space resembles the development known from bulk measurements; in the beginning, selected linear scans or just one plane were analyzed providing a limited amount of information. Later on, adding information from several planes or, even better, measuring a minimum volume in reciprocal space, became the basis to obtain increasingly stable systems of equations.

The scattering close to Bragg reflections was employed for calibration as in the previous investigation of the near-surface microstructure of Pt-48 at. % Rh.[15] Owing to the larger displacements in Ni-Pt alloys, Huang scattering now had to be considered besides thermal diffuse scattering. Its contribution to the total scattering in this range was estimated from bulk measurements. Presumably because of the larger modulation of short-range order scattering, the B value of the Debye-Waller factor was no longer such a sensitive quantity in the fitting procedure, in contrast to the previous in-plane measurement of Ref. 15.

In the diffuse scattering, signs of a noncubic site occupation were noticed for the near-surface microstructure. Their strength depends on the range and amplitude of the oscillatory segregation profile and thus on the closeness to the order-disorder transition temperature. The present finding for the nearest-neighbor site occupation must also be reflected in the enhancement of selected Clapp configurations. For the case where $L1_0$ and $L1_2$ are distinguishable (i.e., for Pt atoms around a Pt atom), the building elements of $L1_0$ and $L1_2$ both showed largest (and comparable) enhancement—$L1_0$ is taken as an extremum of the segregation profile of the (110) surface.

The question whether near-surface microstructure and bulk microstructure differ in Ni-25 at. % Pt may not be finally decided. The present layer-resolved short-range order parameters from *ab initio* calculations indicate that very precise measurements are required to resolve a tetragonal local order within the average over a few ten layers that is accessible from diffuse scattering under grazing incidence. Diffuse scattering shows that at best the nearest-neighbor short-range order parameter might be sensitive to the presence of the segregation profile. A comparison with the bulk microstructure will provide further insight, also with respect to the displacement parameters.

The present first-principles simulations support a finding previously reached on the segregation reversal of Ni-Pt(110) surfaces: it is the segregation of Pt in the second layer together with the strong nearest-neighbor interaction. The strength of the interaction is reflected in the high order-disorder transition temperature of Ni-25 at. % Pt.

ACKNOWLEDGMENTS

The authors are grateful to E. Fischer for his support in growing the single crystal and to FIRST (ETH Zurich) for access to the lapping equipment. They are grateful to P. R. Willmott and the SLS team for assistance in the experiment and the SLS for providing beamtime. B.S. and M.E. also thank J. Löffler for his support and encouragement. This work was partially supported by the "Schweizerischer Nationalfonds zur Förderung der wissenschaftlichen Forschung." A.V.R. is grateful to the Swedish Research Council (VR) and the Swedish Foundation for Strategic Research (SSF) for financial support. Calculations were performed using UPPMAX (Uppsala) and NSC (Linköping) resources.

[1] Y. Gauthier, Surf. Rev. Lett. **3**, 1663 (1996).
[2] Y. Gauthier, R. Baudoing, M. Lundberg, and J. Rundgren, Phys. Rev. B **35**, 7867 (1987).
[3] S. Deckers, F. H. P. M. Habraken, W. F. van der Weg, A. W. Denier van der Gon, B. Pluis, J. F. van der Veen, and R. Baudoing, Phys. Rev. B **42**, 3253 (1990).
[4] Y. Gauthier, R. Baudoing, and J. Jupille, Phys. Rev. B **40**, 1500 (1989).
[5] Y. Gauthier, W. Hoffmann, and M. Wuttig, Surf. Sci. **233**, 239 (1990).
[6] W. Hebenstreit, G. Ritz, M. Schmid, A. Biedermann, and P. Varga, Surf. Sci. **388**, 150 (1997).
[7] M. Schmid, A. Biedermann, S. D. Böhmig, P. Weigand, and P. Varga, Surf. Sci. **318**, 289 (1994).
[8] P. Weigand, B. Jelinek, W. Hofer, and P. Varga, Surf. Sci. **301**, 306 (1994).
[9] G. Kostorz, in *Physical Metallurgy*, edited by R. W. Cahn and P. Haasen (North-Holland, Amsterdam, 1996), p. 1115.
[10] W. Schweika, *Disordered Alloys: Diffuse Scattering and Monte Carlo Simulations* (Springer, Berlin, 1998).
[11] G. E. Ice and C. J. Sparks, Annu. Rev. Mater. Sci. **29**, 25 (1999).
[12] B. Schönfeld, Prog. Mater. Sci. **44**, 435 (1999).
[13] V. M. Nield and D. A. Keen, *Diffuse Scattering from Crystalline Materials* (Clarendon, Oxford, 2001).
[14] M. Kimura, J. B. Cohen, S. Chandavarkar, and K. Liang, J. Mater. Res. **12**, 75 (1997).
[15] Ch. Steiner, B. Schönfeld, M. M. I. P. van der Klis, G. Kostorz, B. D. Patterson, and P. R. Willmott, Phys. Rev. B **73**, 174205 (2006).
[16] D. K. Saha and K.-I. Ohshima, J. Phys.: Condens. Matter **7**, 3203 (1995).
[17] J. A. Rodriguez, S. C. Moss, J. L. Robertson, J. R. D. Copley, D. A. Neumann, and J. Major, Phys. Rev. B **74**, 104115 (2006).
[18] B. Schönfeld, M. Engelke, and A. V. Ruban, Phys. Rev. B **79**, 064201 (2009).
[19] B. Legrand, G. Treglia, and F. Ducastelle, Phys. Rev. B **41**, 4422

(1990).
[20] I. A. Abrikosov, A. V. Ruban, H. L. Skriver, and B. Johansson, Phys. Rev. B **50**, 2039 (1994).
[21] P. Deurinck and C. Creemers, Surf. Sci. **441**, 493 (1999).
[22] L. V. Pourovskii, A. V. Ruban, I. A. Abrikosov, Y. Kh. Vekilov, and B. Johansson, Phys. Rev. B **64**, 035421 (2001).
[23] F. Ducastelle, *Order and Phase Stability in Alloys* (North-Holland, Amsterdam, 1991).
[24] A. V. Ruban, S. Shallcross, S. I. Simak, and H. L. Skriver, Phys. Rev. B **70**, 125115 (2004).
[25] A. V. Ruban and I. A. Abrikosov, Rep. Prog. Phys. **71**, 046501 (2008).
[26] I. A. Abrikosov and H. L. Skriver, Phys. Rev. B **47**, 16532 (1993).
[27] A. V. Ruban and H. L. Skriver, Comput. Mater. Sci. **15**, 119 (1999).
[28] I. A. Abrikosov, A. M. N. Niklasson, S. I. Simak, B. Johansson, A. V. Ruban, and H. L. Skriver, Phys. Rev. Lett. **76**, 4203 (1996).
[29] I. A. Abrikosov, S. I. Simak, B. Johansson, A. V. Ruban, and H. L. Skriver, Phys. Rev. B **56**, 9319 (1997).
[30] A. V. Ruban and H. L. Skriver, Phys. Rev. B **66**, 024201 (2002); A. V. Ruban, S. I. Simak, P. A. Korzhavyi, and H. L. Skriver, *ibid.* **66**, 024202 (2002).
[31] O. K. Andersen, O. Jepsen, and G. Krier, *Lectures on Methods of Electronic Structure Calculation* (World Scientific, Singapore, 1994), p. 63.
[32] L. Vitos, Phys. Rev. B **64**, 014107 (2001); L. Vitos, I. A. Abrikosov, and B. Johansson, Phys. Rev. Lett. **87**, 156401 (2001).
[33] P. E. Blöchl, Phys. Rev. B **50**, 17953 (1994).
[34] G. Kresse and D. Joubert, Phys. Rev. B **59**, 1758 (1999).
[35] G. Kresse and J. Hafner, Phys. Rev. B **48**, 13115 (1993).
[36] G. Kresse and J. Furthmüller, Comput. Mater. Sci. **6**, 15 (1996); Phys. Rev. B **54**, 11169 (1996).
[37] V. L. Moruzzi, J. F. Janak, and K. Schwarz, Phys. Rev. B **37**, 790 (1988).
[38] J. P. Perdew, K. Burke, and M. Ernzerhof, Phys. Rev. Lett. **77**, 3865 (1996).
[39] J. P. Perdew and Y. Wang, Phys. Rev. B **45**, 13244 (1992).
[40] H. J. Monkhorst and J. D. Pack, Phys. Rev. B **13**, 5188 (1976).
[41] W. A. Ferrando, R. Segnan, and A. I. Schindler, Phys. Rev. B **5**, 4657 (1972).
[42] B. L. Gyorffy, A. J. Pindor, J. B. Staunton, G. M. Stocks, and H. Winter, J. Phys. F: Met. Phys. **15**, 1337 (1985).
[43] A. I. Lichtenstein, M. I. Katsnelson, and G. Kotliar, Phys. Rev. Lett. **87**, 067205 (2001).
[44] J. B. Staunton and B. L. Gyorffy, Phys. Rev. Lett. **69**, 371 (1992).
[45] A. V. Ruban, S. Khmelevskyi, P. Mohn, and B. Johansson, Phys. Rev. B **76**, 014420 (2007).
[46] B. D. Patterson, R. Abela, H. Auderset, Q. Chen, F. Fauth, F. Gozzo, G. Ingold, H. Kühne, M. Lange, D. Maden, D. Meister, P. Pattison, Th. Schmidt, B. Schmitt, C. Schulze-Briese, M. Shi, M. Stampanoni, and P. R. Willmott, Nucl. Instrum. Methods Phys. Res. A **540**, 42 (2005).
[47] J. M. Cowley, J. Appl. Phys. **21**, 24 (1950).
[48] G. H. Vineyard, Phys. Rev. B **26**, 4146 (1982).
[49] G. A. Alers, J. R. Neighbours, and H. Sato, J. Phys. Chem. Solids **13**, 40 (1960).
[50] D. T. Cromer, J. Chem. Phys. **50**, 4857 (1969).
[51] *International Tables for Crystallography*, edited by A. J. C. Wilson (Kluwer, Dordrecht, 1992).
[52] S. Sasaki, KEK Report No. 88–14, Tsukuba, Japan, 1989 (unpublished).
[53] B. E. Warren, *X-ray Diffraction* (Dover, New York, 1990).
[54] P. C. Clapp, Phys. Rev. B **4**, 255 (1971).
[55] V. Gerold and J. Kern, Acta Metall. **35**, 393 (1987).
[56] M. A. Krivoglaz, *Diffuse Scattering of X-rays and Neutrons by Fluctuations* (Springer, Berlin, 1996).
[57] P. C. Clapp and S. C. Moss, Phys. Rev. **142**, 418 (1966).
[58] I. V. Masanskii, V. I. Tokar, and T. A. Grishchenko, Phys. Rev. B **44**, 4647 (1991).
[59] T. B. Massalski, *Binary Alloy Phase Diagrams* (ASM International, Materials Park, Ohio, 1990).
[60] D. Paudyal, T. Saha-Dasgupta, and A. Mookerjee, J. Phys.: Condens. Matter **15**, 1029 (2003).